

SIMULATION OF BLOOD FLOW THROUGH AN ARTIFICIAL HEART

Cetin Kiris, I-Dee Chang
Stanford University
Stanford, California

Stuart E. Rogers, Dochan Kwak
NASA Ames Research Center
Moffett Field, California

Abstract

A numerical simulation of the incompressible viscous flow through a prosthetic tilting disk heart valve is presented in order to demonstrate the current capability to model unsteady flows with moving boundaries. Both steady-state and unsteady flow calculations are done by solving the incompressible Navier-Stokes equations in three-dimensional generalized curvilinear coordinates. In order to handle the moving boundary problems, the chimera grid embedding scheme which decomposes a complex computational domain into several simple subdomains is used. An algebraic turbulence model for internal flows is incorporated to reach the physiological values of Reynolds number. Good agreement is obtained between the numerical results and experimental measurements. It is found that the tilting disk valve causes large regions of separated flow, and regions of high shear.

Introduction

Various types of prosthetic heart valves have been used widely as the replacements of natural valves since the first successful valve replacement performed in 1960. However, each of the valve design has some difficulties, which cause the artificial heart valve to be less efficient than the natural one. The difficulties which are related to the nonphysiological flow characteristics of the currently used prosthetic heart valves are: 1) Large pressure losses across the valves prevent the heart working efficiently; 2) Separated and secondary flow regions cause clotting; 3) High turbulent shear stress can damage the red blood cells. Having detailed knowledge of the flow quantities can help a design engineer improve the valve geometry, where a smooth flow is desired. Certain experimental studies¹⁻³ have pointed out the effects of the stagnation and recirculation regions and compared commonly used valve geometries. Since the experimental measurements provide flow characteristics for only certain regions of the flowfield, the numerical simulation of the flow through the artificial heart valve will be extremely helpful in the design and development stage of the prostheses.

Most of the numerical studies modeled the flow through the heart valve devices by excluding the moving boundary problems. Underwood and Mueller⁴ obtained the flow characteristics for Kay-Shiley disk type valve using the stream function-vorticity

formulation. Their results showed agreement with experimental data up to Reynolds number of 600. Idelsohn, Costa, and Ponso⁵ modeled the flow through Kay-Shiley caged disk, Starr-Edwards caged ball, and Bjork-Shiley tilting disk valves and compared their performance. A maximum Reynolds number of 1500 was reached in their numerical study. In the above studies, the caged disk and caged ball geometries are axisymmetric, and the tilting disk geometry is two-dimensional. In actual case, the tilting disk geometry is three-dimensional, the flow through heart valves is unsteady, and Reynolds numbers are as high as 6500. Peskin and McQueen⁶ modeled the prosthetic heart valves in the numerical simulation of the flow in the heart. They used boundary forces derived from the energy function in order to model valve opening and closing, and they also modeled the elastic behavior of the walls. Their solution is obtained for the low Reynolds numbers in two dimensions using square cartesian mesh. McCracken and Peskin⁷ applied a combination vortex-grid method for the blood flow through the mitral valve in two dimensions. This method is applied to the problems in which the solution does not have strong dependence on the Reynolds number. Peskin and McQueen⁸ demonstrates the capability of modeling elastic behavior of the heart muscle by applying their extended three dimensional solution procedure to a toroidal tube. In order to obtain a solution procedure aimed at design improvements in prosthetic heart valves, the computation of steady-state and unsteady flow through the Bjork-Shiley tilting disk valve in three-dimensional configuration with the use of a grid embedding scheme is proposed in the current work. The equations are solved in a curvilinear generalized coordinate system, and the valve opening and closing are simulated by calculating the forces acting on the valve.

One of the biggest difficulties in the simulation of the flows in complicated three-dimensional configurations is the discretization of the physical domain with a single grid. The problem becomes more severe if one body in the domain of interest moves relative to another one as is seen in the tilting disk configuration. The use of a zonal approach⁹ would be a practical solution of the moving boundary problem if the grids could be constrained to common boundaries. The chimera grid embedding technique^{10,11} provides a greater flexibility for the grid motion. Instead of using common boundaries between grids, common regions are used. In the present work, the chimera approach is used to discretize the geometry of the disk valve. In addition, the procedure obtained for the heart valve configuration can be easily utilized for other unsteady incompressible viscous flows with moving boundaries, e.g., flow through Space Shuttle External Tank/Orbiter propellant feed line disconnect flapper valves.

In the first section, the method of solving the incompressible Navier-Stokes equations is described, and the algebraic turbulence model is summarized. Next, the geometry and the use of the chimera scheme are discussed. Following that is a presentation of the computed results obtained from the current approach.

Governing Equations and Method of Solution

The algorithm used in both steady-state and unsteady flow calculations is based on the method of artificial compressibility, which produces a hyperbolic system of equations by introducing a time derivative pressure term into the continuity equation.

The resulting incompressible Navier-Stokes equations can be written in a generalized curvilinear coordinate system (ξ, η, ζ) as follows

$$\frac{\partial Q}{\partial \tau} + \frac{\partial}{\partial \xi}(E - E_v) + \frac{\partial}{\partial \eta}(F - F_v) + \frac{\partial}{\partial \zeta}(G - G_v) = 0 \quad (1)$$

where Q , and convective flux vectors E , F , G are

$$Q = \frac{1}{J} \begin{bmatrix} p \\ u \\ v \\ w \end{bmatrix} \quad E = \frac{1}{J} \begin{bmatrix} \beta U \\ \xi_x p + uU + \xi_t u \\ \xi_y p + vU + \xi_t v \\ \xi_z p + wU + \xi_t w \end{bmatrix}$$

$$F = \frac{1}{J} \begin{bmatrix} \beta V \\ \eta_x p + uV + \eta_t u \\ \eta_y p + vV + \eta_t v \\ \eta_z p + wV + \eta_t w \end{bmatrix} \quad G = \frac{1}{J} \begin{bmatrix} \beta W \\ \zeta_x p + uW + \zeta_t u \\ \zeta_y p + vW + \zeta_t v \\ \zeta_z p + wW + \zeta_t w \end{bmatrix}$$

Here J , β , p , u , v , and w denote the Jacobian of transformation, the pseudocompressibility coefficient, pressure, and velocity components, respectively. The contravariant velocity components U , V , and W are defined as

$$U = \xi_t + \xi_x u + \xi_y v + \xi_z w$$

$$V = \eta_t + \eta_x u + \eta_y v + \eta_z w$$

$$W = \zeta_t + \zeta_x u + \zeta_y v + \zeta_z w$$

For an orthogonal grid assumption, the viscous flux vectors E_v , F_v , and G_v are given by

$$E_v = \frac{1}{ReJ} \begin{bmatrix} (\xi_x^2 + \xi_y^2 + \xi_z^2)u_\xi \\ (\xi_x^2 + \xi_y^2 + \xi_z^2)v_\xi \\ (\xi_x^2 + \xi_y^2 + \xi_z^2)w_\xi \end{bmatrix} \quad F_v = \frac{1}{ReJ} \begin{bmatrix} (\eta_x^2 + \eta_y^2 + \eta_z^2)u_\eta \\ (\eta_x^2 + \eta_y^2 + \eta_z^2)v_\eta \\ (\eta_x^2 + \eta_y^2 + \eta_z^2)w_\eta \end{bmatrix}$$

$$G_v = \frac{1}{ReJ} \begin{bmatrix} (\zeta_x^2 + \zeta_y^2 + \zeta_z^2)u_\zeta \\ (\zeta_x^2 + \zeta_y^2 + \zeta_z^2)v_\zeta \\ (\zeta_x^2 + \zeta_y^2 + \zeta_z^2)w_\zeta \end{bmatrix}$$

where Re is the Reynolds number.

In the steady-state formulation, the time derivatives are differenced using the Euler backward formula. The equations are solved iteratively in pseudo-time until the the solution converges to a steady state. In the time-accurate formulation, the time derivatives in the momentum equations are differenced using a second-order, three-point,

backward-difference formula. The equations are iterated to convergence in pseudo-time for each physical time step until a divergence-free velocity field is obtained. The numerical method uses a second-order central difference for viscous terms and a higher order flux-difference splitting for the convective terms. The ξ derivative of the convective flux E can be written as

$$\frac{\partial E}{\partial \xi} \approx \frac{[E_{i+1/2} - E_{i-1/2}]}{\Delta \xi}$$

The numerical flux $E_{i+1/2}$ is defined as follow

$$E_{i+1/2} = \frac{1}{2} [E(Q_{i+1}) + E(Q_i) - \phi_{i+1/2}] \quad (2)$$

where the $\phi_{i+1/2}$ is a dissipation term. The order of the scheme is determined by the definition of the dissipation term $\phi_{i+1/2}$. For $\phi_{i+1/2} = 0$, the differencing is reduced to a second-order central difference scheme. A first-order upwind flux is defined by

$$\phi_{i+1/2} = (\Delta E_{i+1/2}^+ - \Delta E_{i+1/2}^-) \quad (3)$$

and a third-order upwind flux is given by

$$\phi_{i+1/2} = -\frac{1}{3} (\Delta E_{i-1/2}^+ - \Delta E_{i+1/2}^+ + \Delta E_{i+1/2}^- - \Delta E_{i+3/2}^-) \quad (4)$$

where ΔE^\pm is the flux difference across positive or negative traveling waves, and is computed as

$$\Delta E_{i+1/2}^\pm = A^\pm(\bar{Q}) \Delta Q_{i+1/2}$$

here A^\pm is the plus (minus) Jacobian matrix. The Δ operator, and \bar{Q} are given by

$$\Delta Q_{i+1/2} = Q_{i+1} - Q_i$$

$$\bar{Q} = \frac{1}{2}(Q_{i+1} + Q_i)$$

An implicit delta law form approximation to Eq.(1) after linearization in time and the use of approximate Jacobians of the flux differences results in a 4 x 4 block heptadiagonal matrix equation. The matrix equation is solved iteratively by using a nonfactored line relaxation scheme, which maintains stability and allows a large pseudo-time step to be taken. At each sweep direction, a tridiagonal matrix is formed and off line terms of the matrix equation are moved on the right-hand side of the equation. Details of the numerical method are given in Refs. 12-14.

An algebraic mixing-length turbulence model, which is presented in Ref. 15, is utilized in the present computations. The turbulent eddy viscosity is taken as

$$\nu_t = l^2 |w|$$

where l is the mixing-length, and $|w|$ is the absolute value of vorticity. In order to account the effect of more than one wall in the region close to the tilting disk, the mixing-length is given as

$$1/l = \left(\sum_{k=1}^n 1/(cy_k D_k) \right)$$

where n is the number of walls, $c = 0.4$ is the Von Karman's constant, y_k is the distance from the k^{th} surface, and D_k is the Van Driest damping factor for the k^{th} surface.

Geometry and Grid System

In the Bjork-Shiley tilting disk heart valve, the tilting disk is placed in front of the sinus region of the human aorta. The aortic root has three sinuses about 120 degree apart from one another. The tilting disk valve model used in this computation is simplified by assuming that the sinus region of aorta has a circular cross-section. The cage and struts which hold the free-floating disk inside the sewing ring are not included in the geometry. It is also assumed that the walls do not have an elastic deformation. The computational geometry used in unsteady flow computations is given in Figure 1. The channel length is taken to be five aorta diameters long. The disk motion is illustrated by showing three different positions of the disk. The disk angles shown are 75, 50, and 30 degrees as measured from the centerline of the aorta. The tilting disk is allowed to rotate about the horizontal axis that is 1/6 of a disk diameter below the center of the disk. Because of this asymmetric disk orientation, the flow is three dimensional.

The chimera grid embedding technique, which has been successfully used for external flow problems, has been employed by using two overlapped grids as shown in Figure 2-a. Grid 1 contains 17,199 points which are distributed $63 \times 21 \times 13$ in the ξ , η , and ζ directions. It occupies the whole region in the aorta from entrance to exit, and remains stationary. Grid 2 has 4,725 points as distributed $25 \times 21 \times 9$. It wraps around the tilting disk, and moves with the disk. The lateral symmetry planes of the two grids are shown in Figure 2-b in order to demonstrate how the grid embedding scheme is applied to the present problem. Grid points which lie within the disk geometry and outside the aorta grid are excluded from the solution process. These excluded points are called hole points, and the immediate neighbors of the hole points are called fringe points. The information is passed from one grid to another one via fringe and grid boundary points by interpolating the dependent variables. Tri-linear interpolation is used in the present computations. In order to distinguish the hole and fringe points from regular computational points, an IBLANK array is used in the flow solver. For hole, grid boundary, and fringe points IBLANK is set to zero, otherwise it is set to one. In order to exclude the hole and grid boundary points from the solution procedure at each time step, the ΔQ solution is processed as follows

$$Q^{n+1} = Q^n + \Delta Q * IBLANK$$

Since 3rd order flux-differencing is used for convective terms, the order of differencing needs to be reduced to the second order differencing near the fringe points.

Computed Results

Presented here are the results of steady-state flow and unsteady flow with the disk motion in the configuration mentioned above. The problems are non-dimensionalized by using the entrance diameter as a unit length, and the average inflow velocity as the unit velocity. The geometries used in the steady-state and unsteady calculations are similar to the geometries used in the experimental studies in Ref. 1,2 and Ref. 3 respectively. In order to reduce the computational effort and memory size, the inflow and outflow boundaries are placed a short distance from the region of interest in comparison with the boundaries in the experimental studies. In addition, the exact shape of the sinus region of aorta used in the experiments is not available at present. Because of these differences between experimental and computational configurations, there are small differences between experimental measurements and present computations.

At a viscous no-slip surface, both the velocity and the pressure gradient normal to the wall are specified to be zero. At the inflow boundary, the velocities are specified, and the pressure is determined from the characteristic boundary condition. At the outflow boundary, static pressure is specified, and velocities are calculated from the three characteristic waves traveling out of the computational domain.

Steady-state calculations for the 30 degree disk orientation have been carried out for Reynolds numbers in the range of 2000 to 6000, in which experimental data is available. The Reynolds number is based on the diameter and the mean velocity at the entrance of the channel. Figure 3 shows the convergence history for a Reynolds number of 5972. Both averaged residual and maximum divergence of velocity have dropped ten order of magnitude in 600 iterations. For an overlapped grid application, the convergence is shown to be very fast. The values for grid 1 are drawn with solid lines, and the values for grid 2 are drawn with dashed lines. The computing time per grid point per iteration is about 2×10^{-4} sec. Figure 4 shows the pressure drop across the Bjork-Shiley tilting disk valve at different flow rates of physiological interest. P_1 and P_2 are the pressures at the points located 150 mm, and 20 mm upstream from the disk at the centerline of the channel respectively. In order to compare numerical results with the experimental measurements given in Ref. 2, the numerical results are redimensionalized. The computed and measured axial velocity profiles at 42 mm downstream from the disk are shown in Figure 5. Figure 5-a demonstrates the horizontal plane, where axial velocity profiles are given, through the center of the channel. Axial velocity profiles given in Figures 5-b through 5-d illustrate how the stagnation region, which is created by the tilting disk valve, is dominant in the region of 1.5 disk diameter downstream. The numerical results are shown with dots and the experimental results are shown with triangles. The numerical results compare favorably with the experimental measurements given in Refs. 1-2.

Velocity vectors on the lateral symmetry plane are given in Figure 6 for a Reynolds number of 5972. The flow, which is directed to the upper part of the aorta, generates vortices in the sinus region of the aorta and a large separated region along the lower wall of the aorta. Since separated and low flow regions have potential for thrombus formation, clotting may occur on the upper sinus region and the lower wall of

the aorta. The flow is highly accelerated near the tilting disk and the upper wall. Figure 7 shows vorticity magnitude contours on the surface of the channel, inflow surface, and outflow surface of the disk, respectively. It is assumed that maximum vorticity magnitudes indicate the regions of high shear. The sewing ring surface and the edges of the disk are the regions having maximum vorticity magnitude. The upper wall of the channel also has considerably high vorticity magnitudes.

Unsteady flow calculations have been carried out in order to demonstrate and analyze the flow during disk opening and closing. For the present computation, one cycle of valve opening and closing requires 70 physical time steps. During each time step, subiterations are carried out until maximum divergence of velocity and maximum residual drop below 10^{-3} . The computing time required for one cycle of the valve opening and closing is approximately 5 hr. During the valve opening, inflow velocity is imposed at the entrance of the channel. The inflow velocity is chosen as a sinuous function in time. The forces acting on the disk are calculated, and the disk rotation angle is determined. For large disk rotation angle, some information may be lost between the grids when the grid embedding technique is used. In order to prevent the information loss, the maximum allowed disk rotation angle at each physical time step is taken to be less than three degrees. As soon as the disk reaches its fully opened position, which is 30 degrees measured from the horizontal plane, the flow direction is reversed by imposing the inflow velocity at the exit of the channel.

Figures 9-a through 9-f illustrate the velocity vectors on the lateral symmetry plane at $t/T = 0.13, 0.285, 0.385, 0.53, 0.685,$ and 0.8 respectively. T is a period of one cycle during the valve opening and closing. The velocities are very high in the region between the disk and the channel wall as shown in Figure 9-a. During the disk opening, two vortices are formed at the upper and lower edges of the disk. The flow starts to separate behind the disk and reattaches to the wall as shown in Figure 9-b. The stagnation region behind the disk moves downstream as the disk rotates. Highly skewed velocity profiles are seen downstream from the disk as illustrated in Figure 9-c. The growth of the vortices has also been observed in the sinus region of the aorta while the flow opens the valve. Along the lower wall a separation region is formed. Figure 9-d shows the beginning of the valve closing. At this moment, the location of imposing the inflow velocity is moved from entrance to exit. Major flow near the upper wall of the channel forms a recirculation region downstream from the disk. With the help of this recirculation, the lower wall of the channel becomes the major flow region during the valve closing, and upper wall region becomes the low flow region.

The vorticity magnitude contours on the surface of the channel at $t/T = 0.13, 0.285,$ and 0.385 are shown in Figures 8-a through 8-c in order to indicate the regions of high shear. At the beginning of valve opening, jet-like flow between the sewing ring and the disk cause very high vorticity magnitudes as shown in Figure 8-a. During the disk rotation, the high vorticity region on the upper wall of the channel moves from the sinus region to downstream as seen in Figures 8-a through 8-c. The results of more realistic flow calculations, such as the flow through the Pennsylvania State artificial heart including tilting disk valve opening and closing, will be reported in the future.

Concluding Remarks

The solution procedure for unsteady incompressible viscous flow computations has been extended with the incorporation of the grid embedding approach. This has been used to simulate both steady-state and unsteady flow through a tilting disk valve. The physiological values of the Reynolds number have been achieved with the use of a simple mixing-length turbulence model. The numerical results for 30 degree disk orientation were compared against the experimental data, and good agreement was obtained. The flow during the disk opening and closing were simulated within a reasonable computing time. The present capability of simulating complicated internal flow problems with moving boundaries is demonstrated. The procedure obtained here is quite general and applicable for various types of complicated geometries.

Acknowledgments

This work is partially supported by the NASA Technology Utilization office. Computer time is provided by the Applied Computational Fluids branch of NASA Ames Research Center.

References

- ¹ Yoganathan, A. P., Concoran, W. H. and Harrison, E. C., "In Vitro Velocity Measurements in the Vicinity of Aortic Prostheses," *J. Biomechanics*, Vol 12, pp. 135-152, 1979.
- ² Yoganathan, A. P., Concoran, W. H. and Harrison, E. C., "Pressure Drops Across Prosthetic Aortic Heart Valves Under Steady and Pulsatile Flow," *J. Biomechanics*, Vol 12, pp. 153-164, 1979.
- ³ Figliola, R. S. and Mueller, T. J., "On the Hemolytic and Thrombogenic Potential Occluder Prosthetic Heart Valves from In-Vitro Measurements," *J. Biomech. Engng.*, Vol 103, pp. 83-90, 1981.
- ⁴ Mueller, T. J., "Application of Numerical Methods in Physiological Flows," *Numerical Methods in Fluid Dynamics*, 1978
- ⁵ Idelsohn, S. R., Costa, L. E. and Ponso, R., "A Comparative Computational Study of Blood Flow Through Prosthetic Heart Valves Using the Finite Element Method," *J. Fluid Dynamics*, Vol 18, No 2, pp. 97-115, 1985.
- ⁶ Peskin, S. C., McQueen, D. M., "Modeling Prosthetic Heart Valves for Numerical Analysis of Blood Flow in the Heart," *J. Comp. Physics*, Vol 37, pp. 113-132, 1980.
- ⁷ McCracken, M. F., Peskin, S. C. "A Vortex Method for Blood Flow Through Heart Valves," *J. Comp. Physics*, Vol 35, pp. 183-205, 1980.
- ⁸ Peskin, S. C., McQueen, D. M., "A Three-Dimensional Computational Method for the Blood Flow in the Heart," *J. Comp. Physics*, Vol 81, pp. 372-405, 1989.
- ⁹ Rai, M. M. "Unsteady Three-Dimensional Navier-Stokes Simulations of Turbine Rotor-Stator Interaction," AIAA Paper No. 87-2058, 1987.

- ¹⁰ Dougherty, F.C., Benek, J. A., and Steger, J.L., "On Applications of Chimera Grid Schemes to Store Separation," NASA Techn. Memorandum 88193, 1985.
- ¹¹ Benek, J. A., Buning, P.G. and Steger, J.L., "A 3-D Chimera Grid Embedding Technique," AIAA Paper No. 85-1523, 1985.
- ¹² Rogers, S. E. and Kwak, D., "An Upwind Differencing Scheme For the Time-Accurate Incompressible Navier-Stokes Equations," AIAA Paper No. 88-2583, 1988.
- ¹³ Rogers, S. E., Kwak, D. and Kiris, C., "Numerical Solution of the Incompressible Navier-Stokes Equations for Steady-State and Time-Dependent Problems," AIAA Paper No. 89-0463, 1989.
- ¹⁴ Rogers, S. E., Kutler, P., Kwak, D. and Kiris, C., "Numerical Simulation of Flow Through an Artificial Heart." NASA Techn. Memorandum 102183, 1989.
- ¹⁵ Burke, R. W. "Computation of Turbulent Incompressible Wing-Body Junction Flow," AIAA Paper No. 89-0279, 1989.

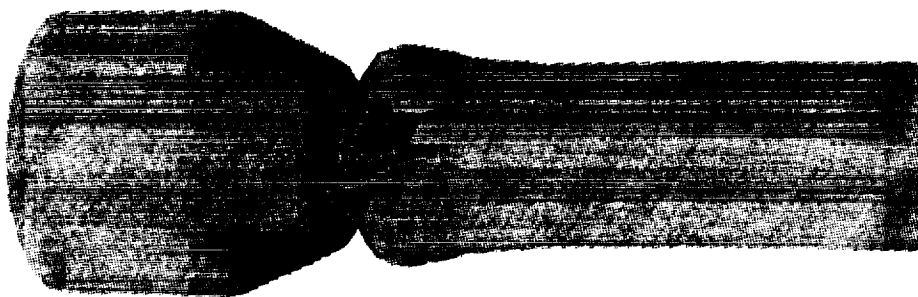


Figure 1. Tilting disk geometry showing valve opening.

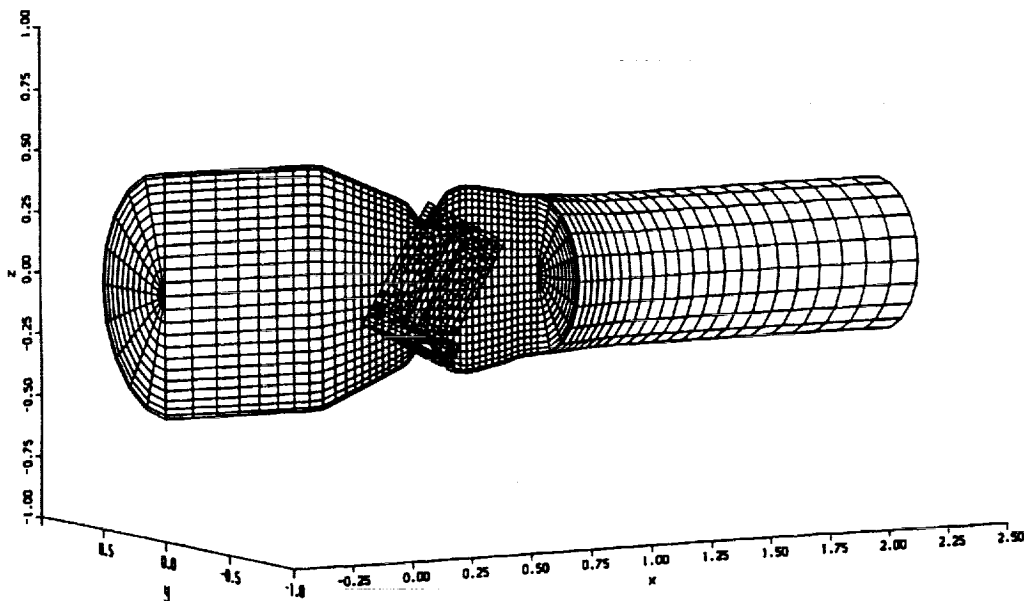


Figure 2. a) Perspective view of two overlapped grids.

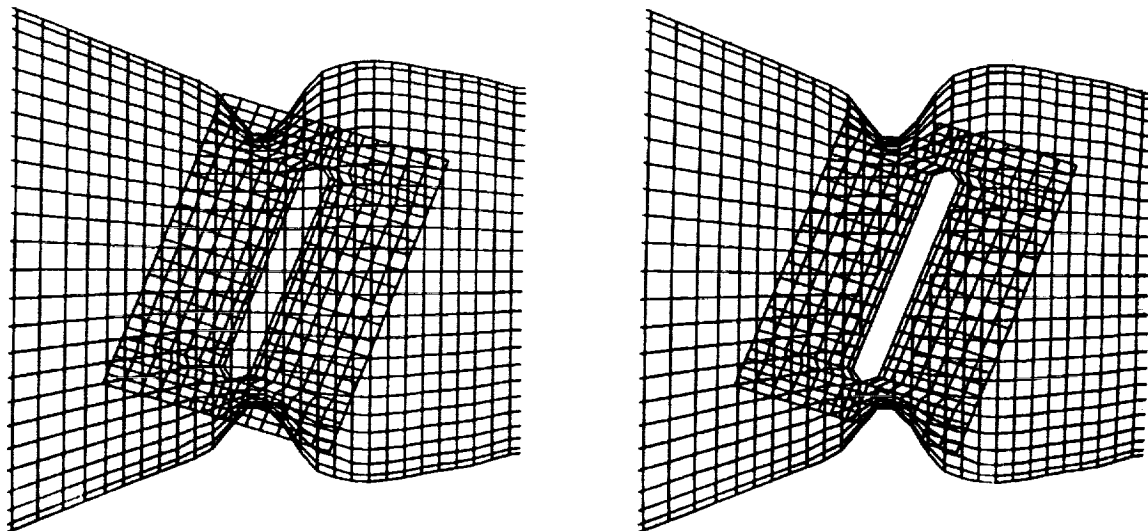


Figure 2. b) Side views of two overlapped grids before and after the hole points are excluded.

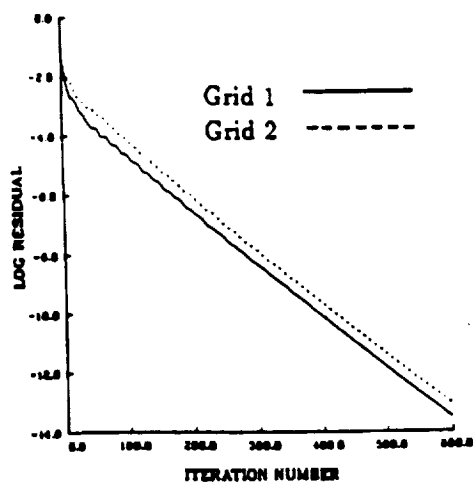
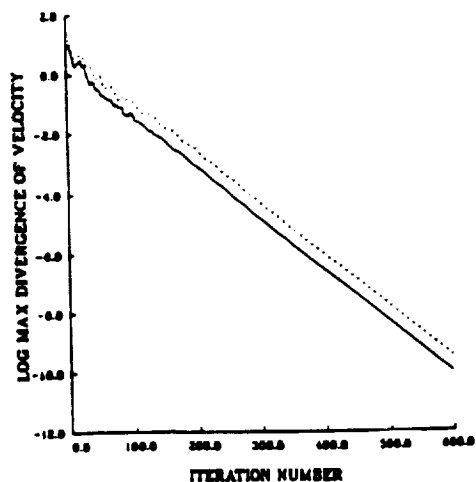


Figure 3. Convergence history for $Re = 5972$.

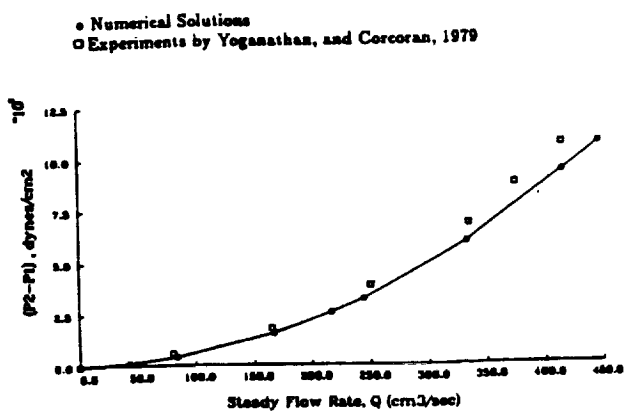
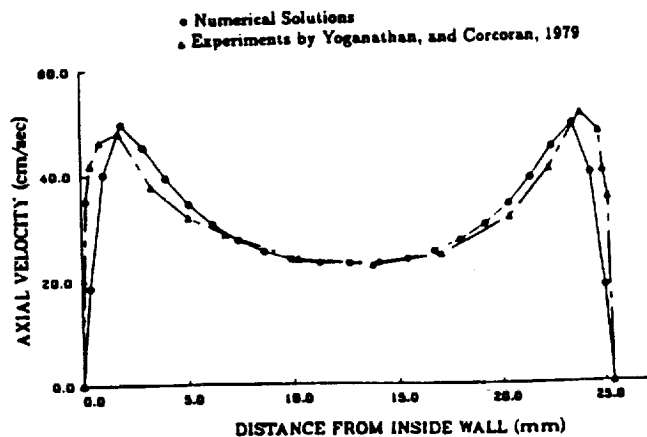
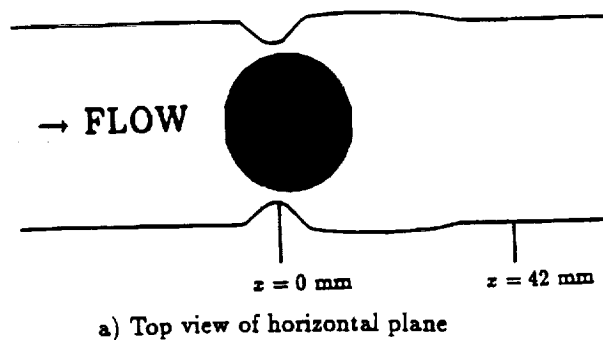
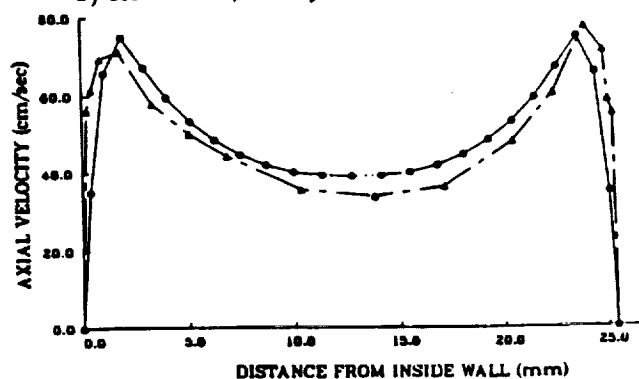


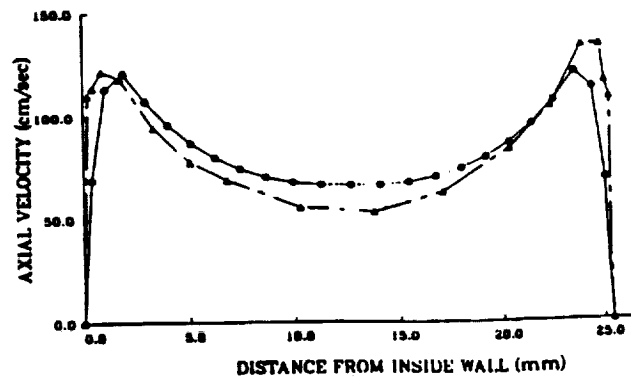
Figure 4. Pressure drop across the tilting disk valve versus steady-state flow rate.



b) $Re = 2390$, Steady flow rate = $167 \text{ cm}^3/\text{sec}$.



c) $Re = 3580$, Steady flow rate = $250 \text{ cm}^3/\text{sec}$.



d) $Re = 5972$, Steady flow rate = $417 \text{ cm}^3/\text{sec}$.

Figure 5. Top view of horizontal plane and axial velocity profiles on the horizontal plane for different flow rates.

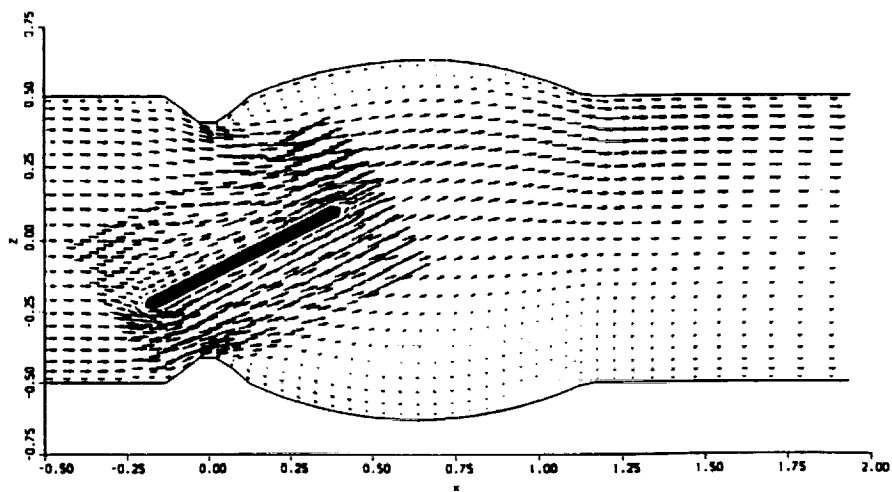


Figure 6. Side view of velocity vectors on the vertical plane.

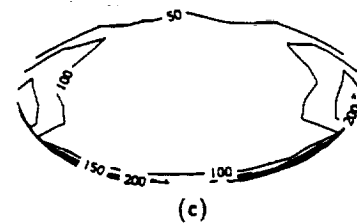
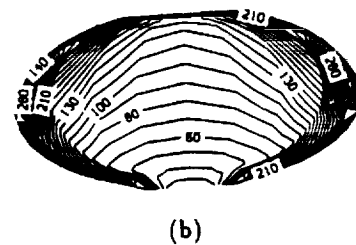
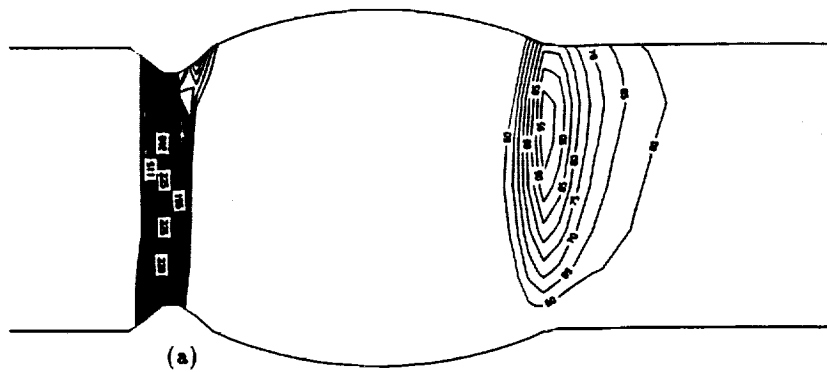


Figure 7. Vorticity magnitude contours on the a) channel surface, b) inflow surface of the disk, c) outflow surface of the disk.

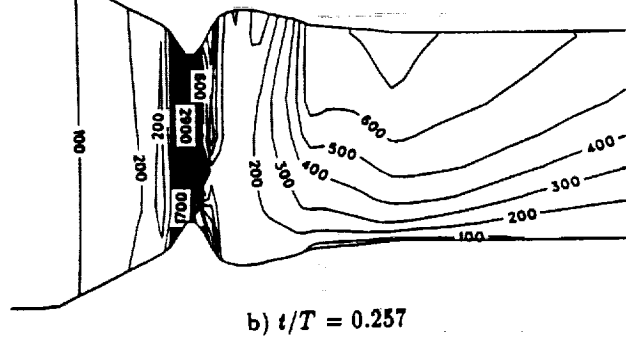
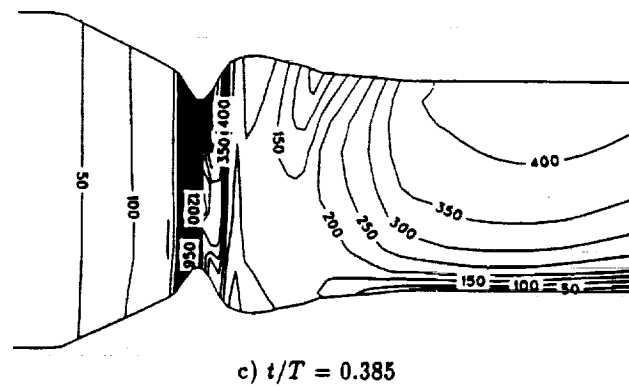
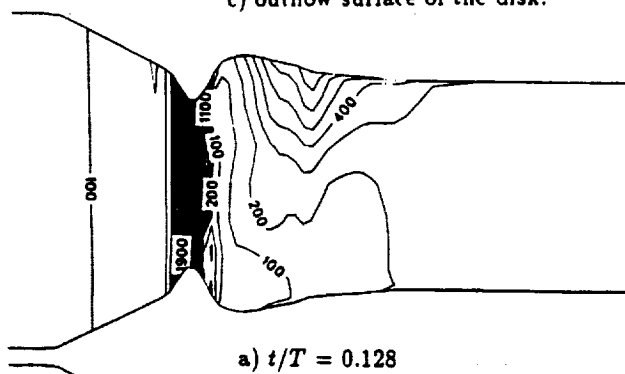
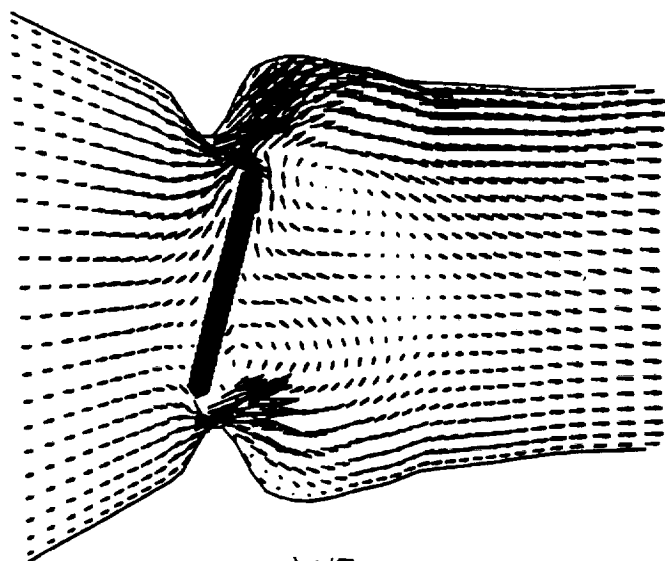
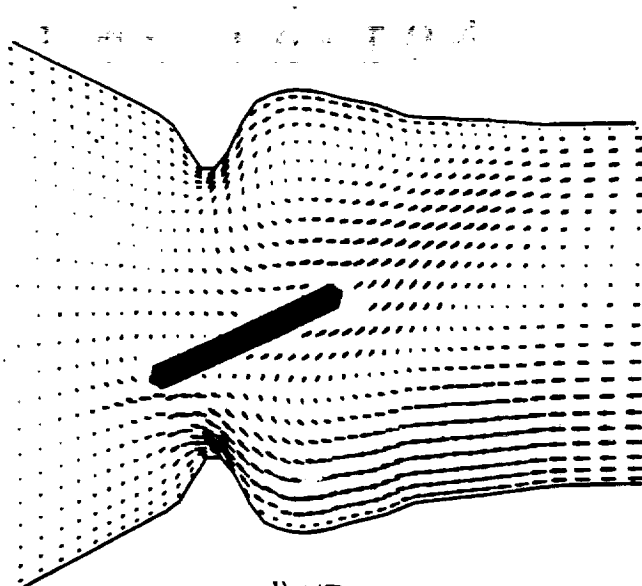


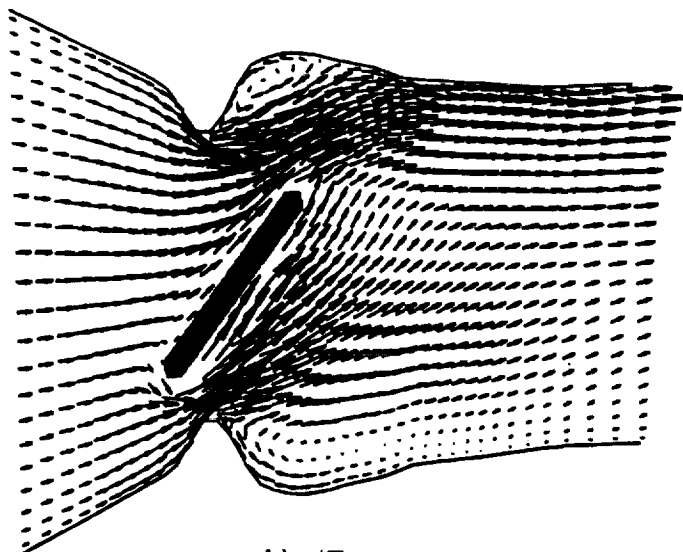
Figure 8. Vorticity magnitude contours on the channel surface during the valve opening.



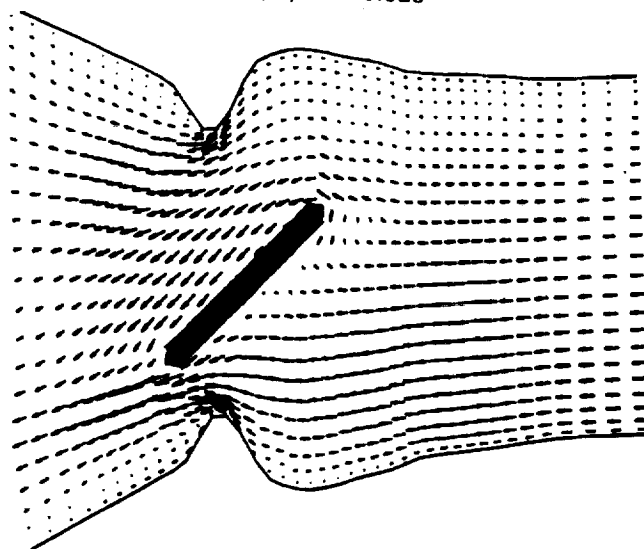
a) $t/T = 0.128$



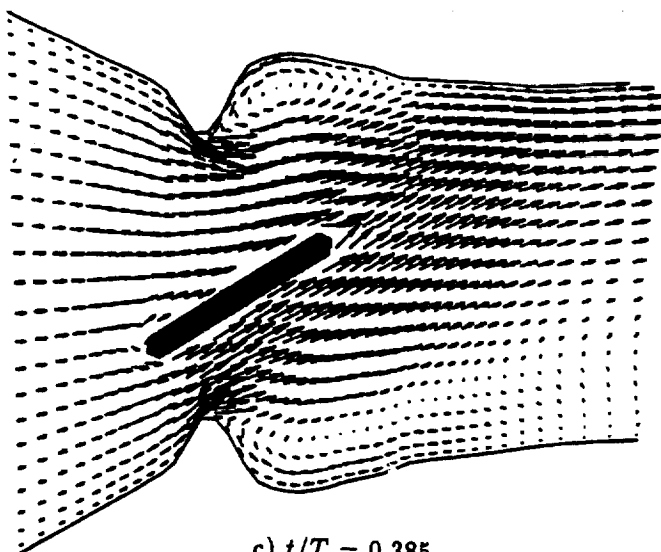
d) $t/T = 0.528$



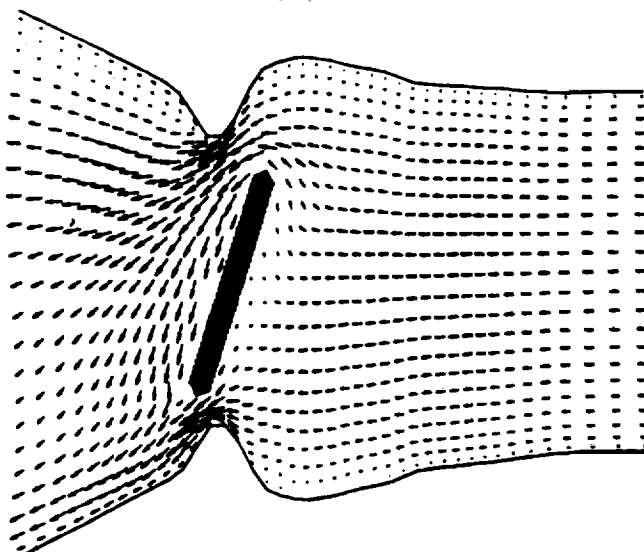
b) $t/T = 0.257$



e) $t/T = 0.685$



c) $t/T = 0.385$



f) $t/T = 0.857$

Figure 9. Side view of velocity vectors on the vertical plane showing the valve opening and closing